Journal of Metals, Materials and Minerals, 35(1), e2228, 2025

Efficacy of $BiFeO_3$ and $Bi_4Ti_3O_{12}$ towards photocatalytic degradation of MG and MB dyes: A comparative study under solar irradiation

Rasmirekha PATTANAIK[1], Rishabh KAMAL[1], Debapriya PRADHAN[1], and Suresh Kumar DASH[1,*]

[1] *Department of Chemistry, ITER, Siksha 'O' Anusandhan (Deemed to be University), Bhubaneswar, Odisha 751030, India*

***Corresponding author e-mail**: sureshdash@soa.ac.in

Received date:
16 December 2024
Revised date:
30 December 2024
Accepted date:
25 January 2025

Keywords:
$BiFeO_3$;
$Bi_4Ti_3O_{12}$;
Dyes;
Kinetics;
Mechanism

Abstract

Bismuth-based perovskite material has been used as promising photocatalysts for photo catalytic degradation of toxic dyes with tailored crystallites and fine-tuned band gap for superior activity. $BiFeO_3$ and $Bi_4Ti_3O_{12}$ were synthesized by a simple sol-gel method and their crystal structure, morphology, and optical property were characterized by XRD, SEM, TEM, FTIR, EDS and UV–DRS. The XRD pattern exhibits the formation of rhombohedral and orthorhombic phase of bismuth ferrite and bismuth titanate. The study confirms the formation of non-uniform $BiFeO_3$ and $Bi_4Ti_3O_{12}$ nanoparticles with uniform particle distribution, with band gap energy (E_g) of 2.2 eV and 2.9 eV, respectively, from UV-DRS analyses and Tauc Plot. The study examined the photocatalytic degradation of a prepared catalyst for MG and MB dyes by altering parameters like solution pH, catalyst dose, and agitation time. The results indicated that $BiFeO_3$ exhibited higher degrading efficiency compared to $Bi_4Ti_3O_{12}$ under similar experimental conditions. $BiFeO_3$ degraded more than ≅ 80% of both MG and MB dyes with 0.4 $mg{\cdot}L^{-1}$ within 90 min compared to more than ≅ 74% for $Bi_4Ti_3O_{12}$ having 0.6 $mg{\cdot}L^{-1}$ catalyst taken in 20 mL of 20 ppm dye concentration in 60 min with prevailing parameter conditions. The higher efficacy of $BiFeO_3$ may be contributed to the E_g that makes the catalyst more active under solar spectrum. The degradation mechanism involved photoinduced electron/hole pairs producing active radical species, with kinetics following a pseudo-first order rate and photocatalyst stability studied through five continuous runs. The study found that $BiFeO_3$ outperforms $Bi_4Ti_3O_{12}$ in reducing cationic dyes and suggests them as potential waste water treatment alternatives.

1. Introduction

The excessive use of dyes, solvents, herbicides, and pesticides in industries like textiles, paint, petrochemicals, and agriculture has raised global environmental concerns. These organic pollutants contaminate water sources and threaten aquatic ecosystems. Addressing these hazardous contaminants is crucial, and there is an urgent need for low-cost, effective methods to treat industrial wastewater containing non-decomposable organic materials. Photocatalytic technology is vital for reducing energy consumption by using solar energy, with the development of high-performance photocatalysts being essential [1,2]. Photocatalytic degradation offers an efficient, cost-effective solution for detoxifying pollutants, including those in drinking water. Methylene blue (MB) and Malachite green (MG), commonly used industrial dyes, serve as benchmark materials for testing adsorbents, though they pose carcinogenic, teratogenic, and mutagenic risks [3-6]. Bismuth-based materials are economical, structurally flexible, and efficient in utilizing sunlight for photocatalysis, making them ideal for energy and environmental applications. These photocatalysts are notable for their environmental safety, versatility, and consistent performance under visible light [7-9]. Perovskite compounds like $Bi_4Ti_3O_{12}$, $BaTiO_3$, $BiFeO_3$, $ZnTiO_3$, $CaTiO_3$, and $SrTiO_3$ are used in fuel cells, sensors, memory devices, and spintronics due to their ferroelectric and piezoelectric properties. These materials are effective alternatives to metal oxides because of their non-toxicity, chemical stability, and strong photocatalytic activity in the visible spectrum [10,11]. This study focuses on comparing the structural, optical, and photocatalytic properties of two perovskite materials, $Bi_4Ti_3O_{12}$, and $BiFeO_3$.

Bismuth titanate is a semiconductor with a large band gap and exists in various crystal phases, including the sillenite ($Bi_{12}TiO_{20}$), ferroelectric perovskite ($Bi_4Ti_3O_{12}$), and pyrochlore ($Bi_2Ti_2O_7$) phases [12-14]. Due to its high dielectric constant, ferroelectric properties, and electro-optical capabilities, it is suitable for applications in storage devices, sensors, piezoelectric ceramics, and optical components [15]. $Bi_4Ti_3O_{12}$, in particular, has gained attention for its photocatalytic potential in removing organic dyes [16]. Bismuth ferrite ($BiFeO_3$), known for its non-toxicity, cost-effectiveness, stability, and electro-optical properties, is also an efficient photocatalyst, especially in organic dye degradation [17,18]. Various methods, such as co-precipitation, sol-gel, and hydrothermal synthesis, are used to prepare bismuth titanate and bismuth ferrite nanostructures [11,19,20].

The sol-gel method was used to produce both bismuth titanate and bismuth ferrite nanostructures due to its affordability, speed, safety, and ease. Recent studies have focused on their photocatalytic properties. This research aims to identify Bi-based perovskite compounds that

enhance photocatalytic efficiency under solar light and compare the performance of bismuth titanate and bismuth ferrite. The results showed that bismuth ferrite nanostructures, with a smaller band gap of 2.4 eV compared to 2.9 eV for bismuth titanate, exhibited stronger photocatalytic activity when tested on Methylene blue and Malachite green.

2. Materials and methods

2.1 Reagents

Bismuth nitrate hexahydrate ($Bi(NO_3)_3.5H_2O$) (M.W. 485.07 $g{\cdot}mol^{-1}$), Titanium oxide (TiO_2) (M.W. 79.87 $g{\cdot}mol^{-1}$), Oxalic acid dihydrate ($HOOC\text{-}COOH.2H_2O$) (M.W. 126.07 $g{\cdot}mol^{-1}$), Ferric nitrate nonahydrate $Fe(NO_3)_3{\cdot}9H_2O$ (M.W. 404 $g{\cdot}mol^{-1}$), Acetic acid (CH_3COOH) (M.W. 60.052 $g{\cdot}mol^{-1}$), Ammonia solution about 25% (NH_3) (M.W. 17.03 $g{\cdot}mol^{-1}$) were purchased from Merck used as a precursor to synthesized perovskite photocatalysts. The stimulated water contaminants such as Malachite Green (M.W. 927.02 $g{\cdot}mol^{-1}$) and Methylene blue (M.W. 319.85 $g{\cdot}mol^{-1}$) dyes were obtained from Merck. All the chemicals used in this research work were of analytical grade and employed without additional purification. Double distilled and de-ionized water was used for preparing solutions and carrying-out the experiments.

2.2 Characterization

The study used several instruments for characterization: the INSPECT S50 microscope for SEM measurements, the IRAFFINTT-2 spectrometer for FTIR analysis (4000 cm^{-1} to 400 cm^{-1}), and a Shimadzu X-ray diffractometer-7000 for XRD analysis (5° to 60° 2θ at $2°{\cdot}min^{-1}$). Optical properties of the photocatalyst were assessed with a UV-VIS spectrophotometer, while high-resolution transmission electron microscopy (HRTEM) was conducted using a Tecnai G2 20 S-TWIN-FE with resolutions of 0.24 nm and 0.14 nm.

2.3 Synthesis of bismuth ferrite

A translucent solution was created by combining $Bi(NO_3)_3{\cdot}6H_2O$ and $Fe(NO_3)_3{\cdot}9H_2O$ with the necessary amount of acetic acid and water. The aforementioned solution was subsequently treated with the required quantity of citric acid. The solution was agitated for an hour before being evaporated at 70°C for 2 h. The solution was then centrifuged and carefully rinsed with distilled water until the pH was neutral. The precipitate was oven-dried at 70°C overnight and then calcined in a muffle furnace at 500°C for 4 h [11] and collected in a sample tube. $BiFeO_3$ denoted as BFO. The synthesis scheme mentioned below in scheme 1.

2.4 Synthesis of bismuth titanate

The $Bi_4Ti_3O_{12}$ was synthesized using the sol-gel method as outlined in previous research [21]. In brief, 0.2 M of $Bi(NO_3)_3{\cdot}5H_2O$ was placed in a 500 mL beaker and stirred while adding an equal amount of TiO_2 under continuous stirring. To break down any TiO_2 agglomerates, the suspension was sonicated for 10 min at room temperature. Next, a 0.4 M solution of oxalic acid dihydrate was slowly added dropwise under constant, vigorous stirring. Following this, 0.1 M ammonia solution was gradually introduced to the mixture until the pH reached 6 to 7. In this solution, bismuth oxalate was precipitated onto the surface of fine TiO_2 particles via heterogeneous nucleation. The resulting precipitate was thoroughly washed with deionized water and subsequently dried at 40°C for 8 h in a vacuum oven. The precursor was then annealed at 400°C for 5 h, allowed to cool to room temperature, ground using a mortar and pestle, and finally, the $Bi_4Ti_3O_{12}$ nanocomposite (referred to as BTO here after) was obtained. A schematic diagram of this process is shown below in Scheme 2.

2.5 Photocatalytic degradation experiments

BFO and BTO nanoparticles were synthesized to study the photocatalytic degradation of methylene blue (MB) and malachite green (MG) dyes under sunlight with a light intensity of 10000 lux (measured by using a light meter (LX-101A) on the month of September. The effects of pH (3 to 11), catalyst dosage (20 mg to 100 mg), and agitation time on degradation efficiency were examined using 100 mL of dye solution. To enhance dye adsorption, the dye solution was mixed with the photocatalyst and left in the dark for 30 min before being exposed to sunlight for photocatalytic degradation. After a set time, samples were taken, centrifuged, and the supernatant analyzed via UV-Vis spectroscopy to determine degradation efficiency using a specific Equation (1) [22]:

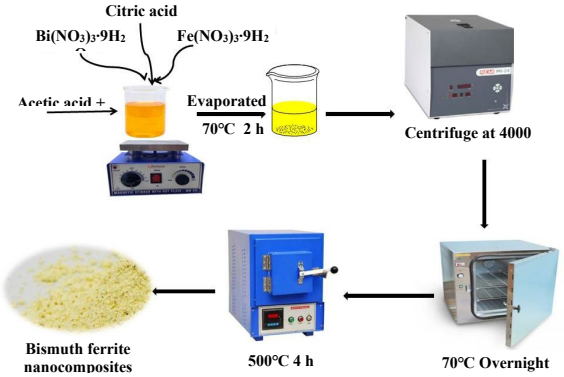

Scheme 1. Schematic illustration of the synthesis of BFO using the sol-gel technique.

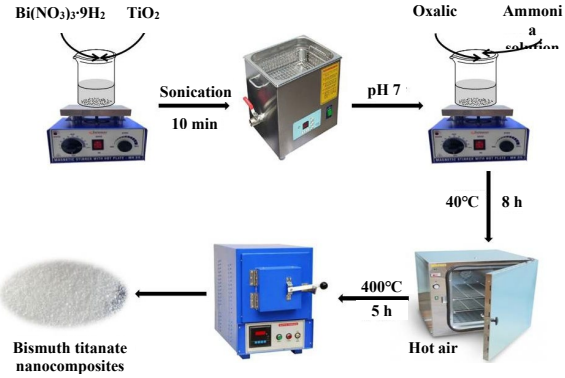

Scheme 2. Schematic representation of the BTO synthesis process using the sol-gel technique.

$$\% \text{ degradation efficiency} = (C_0 - C_t)/C_0 /100 \quad (1)$$

Where C_t ($mg{\cdot}L^{-1}$) is the concentration of each time period and C_0 ($mg{\cdot}L^{-1}$) is the initial concentration.

3. Results and discussion

3.1 Materials characterization

The crystallinity of the samples was evaluated using X-ray diffraction. Bismuth titanate and bismuth ferrite nanoparticles with well crystalline structure were produced showed in Figure 1. The XRD patterns' diffraction peaks correspond to BTO, as described in JCPDS file (JCPDS card number 35-0795), showing that the produced powders are monophasic bismuth titanate with an orthorhombic structure [23]. The diffraction peaks of pure BFO are in good agreement with pure rhombohedral phase, as mentioned in JCPDS file. (JCPDS 71-2494) [24]. Table 1 summarizes the key peaks at 2θ values and provides cell parameters based on both the photocatalysts investigation.

The average crystallite size of the nanostructures was estimated using Scherer's Equation (2).

$$D = k\lambda / \beta\cos\theta \quad (2)$$

In Equation (2), D, θ, β, and λ represent mean crystalline size, Bragg's angle, FWHM of the diffraction peak, and wavelength, respectively [25].

FTIR spectroscopy was used to confirm the structural properties of BFO and BTO nanostructures and identify functional groups on their surfaces. The BFO spectrum showed notable absorption peaks at 440 cm^{-1} (Fe-O bending) and around 539 cm^{-1} (FeO_6 octahedral group) [25,26]. The BTO spectrum displayed absorption bands below 830 cm^{-1}, reflecting its cationic nature, with Ti-O stretching vibrations at 817 cm^{-1} and 588 cm^{-1}. The observed bands differed from those in existing literature, possibly due to differences in particle size, as larger particles typically exhibit lower frequency vibrations and wave numbers [27].

FESEM and TEM were used to analyze the surface morphology and particle size of Bi-based perovskite materials. Figure 3(a) shows the FESEM image of BFO, revealing irregular particles around 200 nm along with flake-shaped particles made of BFO nanoparticles [28]. In Figure 3(b), the SEM micrographs of BTO show nanometric particles forming soft agglomerates after annealing. The particles exhibit an elongated, plate-like morphology typical of BTO powders due to their anisotropic structure [29]. Figure 3(c-d) present HRTEM images of BFO and BTO nanoparticles, respectively. Figure 3(c) shows well-dispersed, fine, and uniform spherical BFO nanoparticles on a copper grid with minimal aggregation. The corresponding selected area electron diffraction (SAED) pattern in Figure 3(e) confirms the well-crystallized, pure rhombohedral crystal structure of BFO, with an inter-planar spacing of 2 Å, consistent with previous studies [30]. Figure 3(d) shows the HRTEM image of BTO nano particles near the edge, verifying their orthorhombic crystallinity with a periodic fringe spacing of 3 Å. The SAED pattern of BTO is shown in Figure 3(f) [31]. Additionally, the EDX spectra of BFO and BTO nano powders are displayed in Figure 3(g-h).

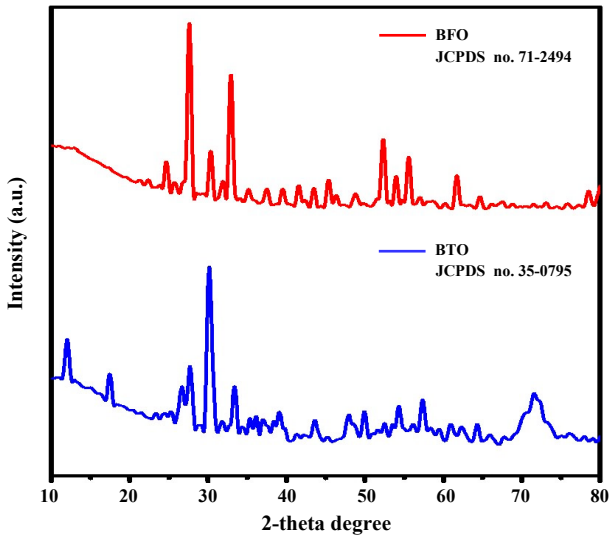

Figure 1. XRD patterns of Bismuth Titanate and Bismuth Ferrite with JCPDS reference.

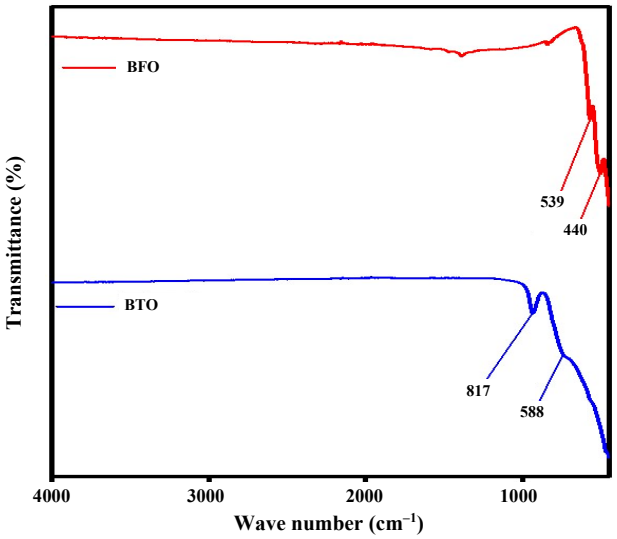

Figure 2. FTIR analysis of BFO and BTO nanoparticles.

Table 1. Summary of the major information gained from the examination of the XRD spectra for the distinct structures: crystalline system, space group, cell characteristics, peaks and the related crystal planes.

	Crystal system	Crystal size	a [Å]	b [Å]	Main peaks at 2θ	Crystal planes
BFO	Rrhombohedral	24.41	5.5781	5.5781	22.3, 31.7, 32.1, 39.4, 51.2, 56.8, 66.9, 71.2, 75.5	(012), (104), (110), (202), (116), (214), (220), (036), (128)
BTO	Orthorhombic	47.40	5.4489	32.8150	30.2, 32.84, 37.06, 47.32, 39.67, 57.24	(171), (200), (062), (202), (280), (170)

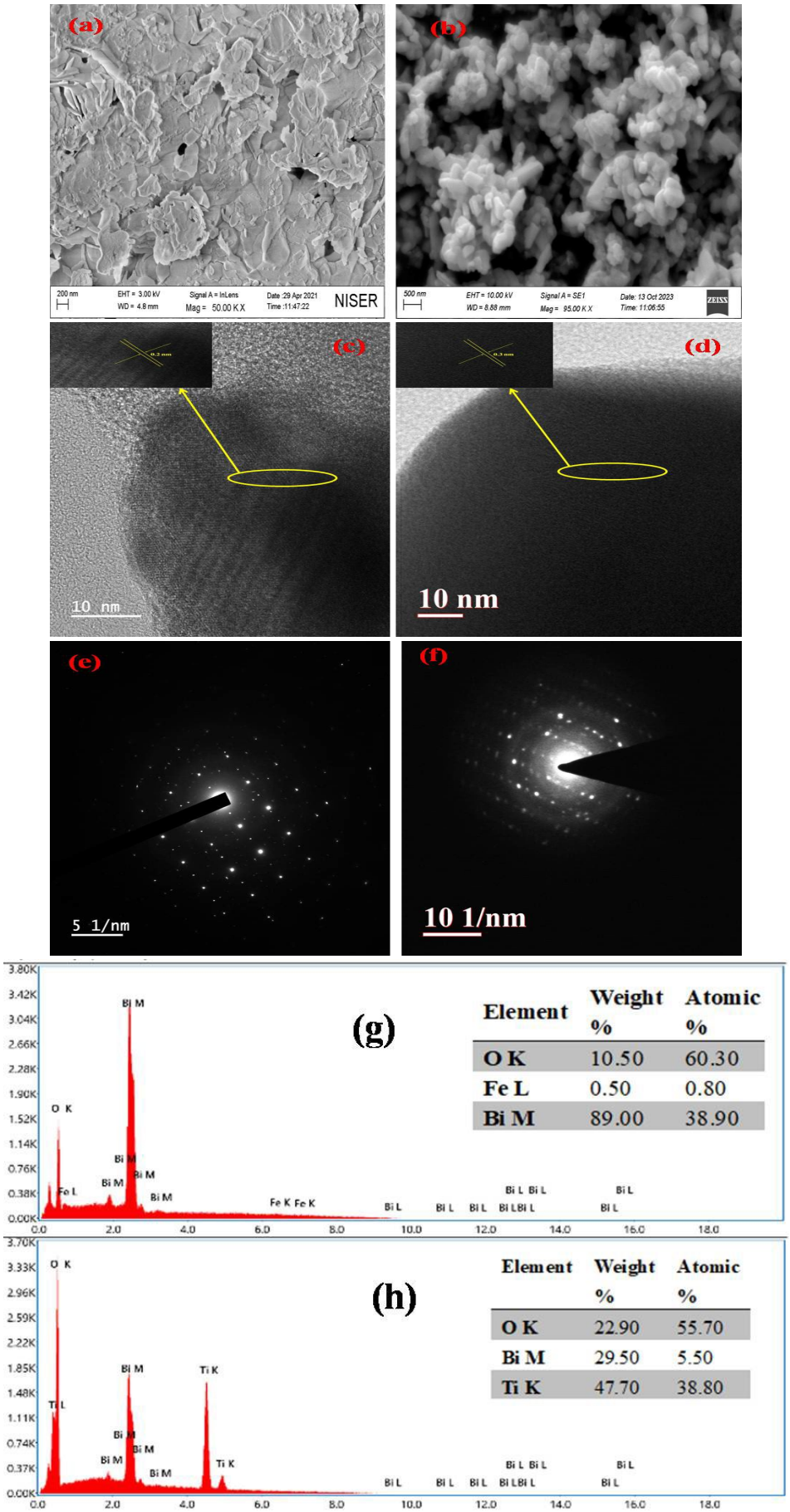

Figure 3. SEM and TEM images of BFO (a, c) and BTO (b, d), SAED patterns for BFO (e), and BTO (f), EDS spectra BFO (g), and BTO (h).

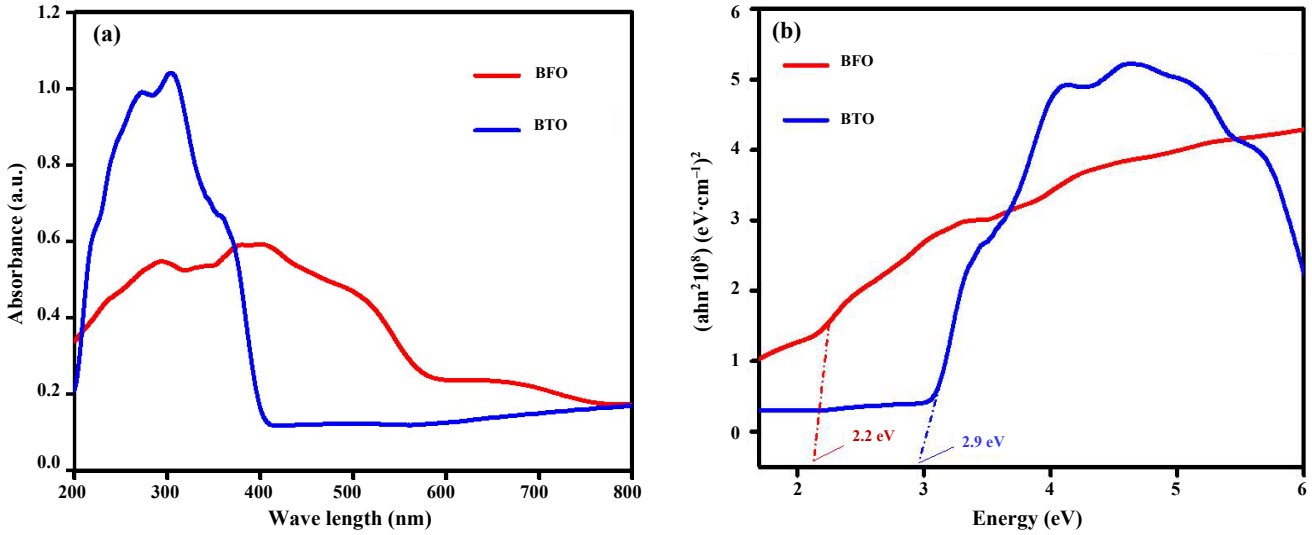

Figure 4. UV-visible absorption spectra of BFO and BTO (a). The Tauc plots for the BFO and BTO nanocomposite (b).

UV-Vis absorption spectroscopy was used to analyze the optical absorption behaviour of the synthesized photocatalysts, with results shown in Figure 4. As shown in Figure 4(a), pure BFO composites have an extended absorption range into the visible spectrum compared to pure BTO. The optical absorption of a semiconductor is influenced by its band gap energy, which was calculated for BFO and BTO catalysts using the intercept method on a plot of $(h\upsilon)^{1/2}$ vs. photon energy. The band gaps were found to be 2.2 eV for BFO and 2.9 eV for BTO, as illustrated in Figure 4(b). The calculations are based on Equation (3) [32].

$$(\alpha h\upsilon)\, n = k\,(h\upsilon - E_g) \qquad (3)$$

In this context, hhh represents the absorption energy, E_g is the band gap energy, k is the effective mass parameter for the valence and conduction bands, and nnn is set to 2 for an indirect transition. To determine the conduction band edge (ECB) of a semiconductor at zero charge, equation 4 provides the necessary formula [33].

$$E_{CB} = X - Ee - 0.5\, E_g \qquad (4)$$

Where E_{CB} is the CB edge potential and X is the absolute electro-negativity of the semiconductor. On the hydrogen scale, Ee denotes the energy of free electrons. E_g denotes a semiconductor's band gap energy. The formula for calculating E_{VB} is $E_{VB} = E_{CB} + E_g$.

The N_2 adsorption-desorption isotherm of the fabricated ferrite hybrid composite was analyzed and is presented in Figure 5. According to the IUPAC classification, the isotherm corresponds to a type IV curve, indicating the characteristics of the composites [34]. The BET surface areas of BFO and BTO were measured to be 12.57 $cm^3 \cdot g^{-1}$ and 7.80 $cm^3 \cdot g^{-1}$ respectively. The increased surface area of the photocatalyst enhances its interaction with organic contaminants on the photocatalyst surface, thereby improving its photocatalytic performance.

X-ray photoelectron spectroscopy (XPS) is a surface-sensitive analytical technique used to determine the formal oxidation states of elements within a composite. In this study, XPS analysis was conducted to examine the inner electronic states of the elements (Ti, O, Bi, and Fe) present in the synthesized BFO and BTO samples. Figure 6 presents the Gaussian curve fitting of the XPS survey spectra for pure BFO and BTO composite. For BTO, the Bi 4f spectrum exhibited spin-orbit splitting into two distinct peaks, located at binding energies of 163 eV and 158 eV, corresponding to Bi $4f_{5/2}$ and Bi $4f_{7/2}$, respectively. These peaks are characteristic of Bi (III), as reported in the literature. In the Ti 2p region, peaks were detected at binding energies of 465.2 eV and 457.5 eV, corresponding to Ti $2p_{1/2}$ and Ti $2p_{3/2}$, respectively, confirming the presence of Ti^{4+} ions in $Bi_4Ti_3O_{12}$.The O 1s region revealed a primary peak at approximately 528.8 eV, attributed to bridging oxygen atoms from Bi–O and Ti–O bonds, consistent with the O 1s peak positions in BiOX and TiO_2 surfaces. A minor peak at around 531 eV was also observed, indicating the presence of hydroxyl groups adsorbed on the surface. These characteristic peaks are as reported in the literature [35].

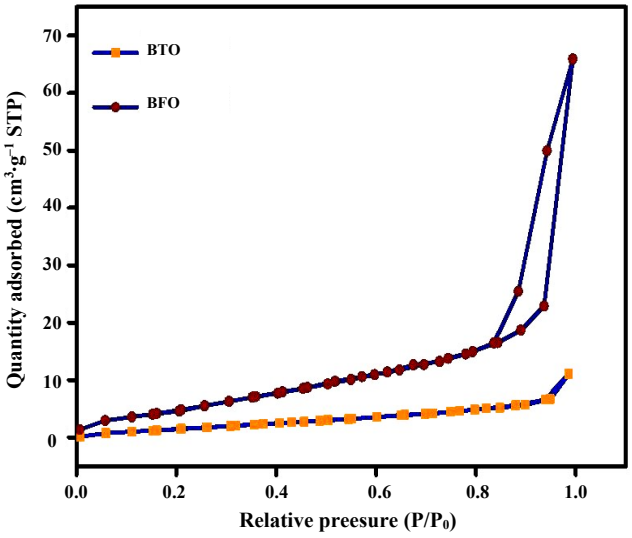

Figure 5. BET analysis data of BFO and BTO satisfying type-(IV) isotherm.

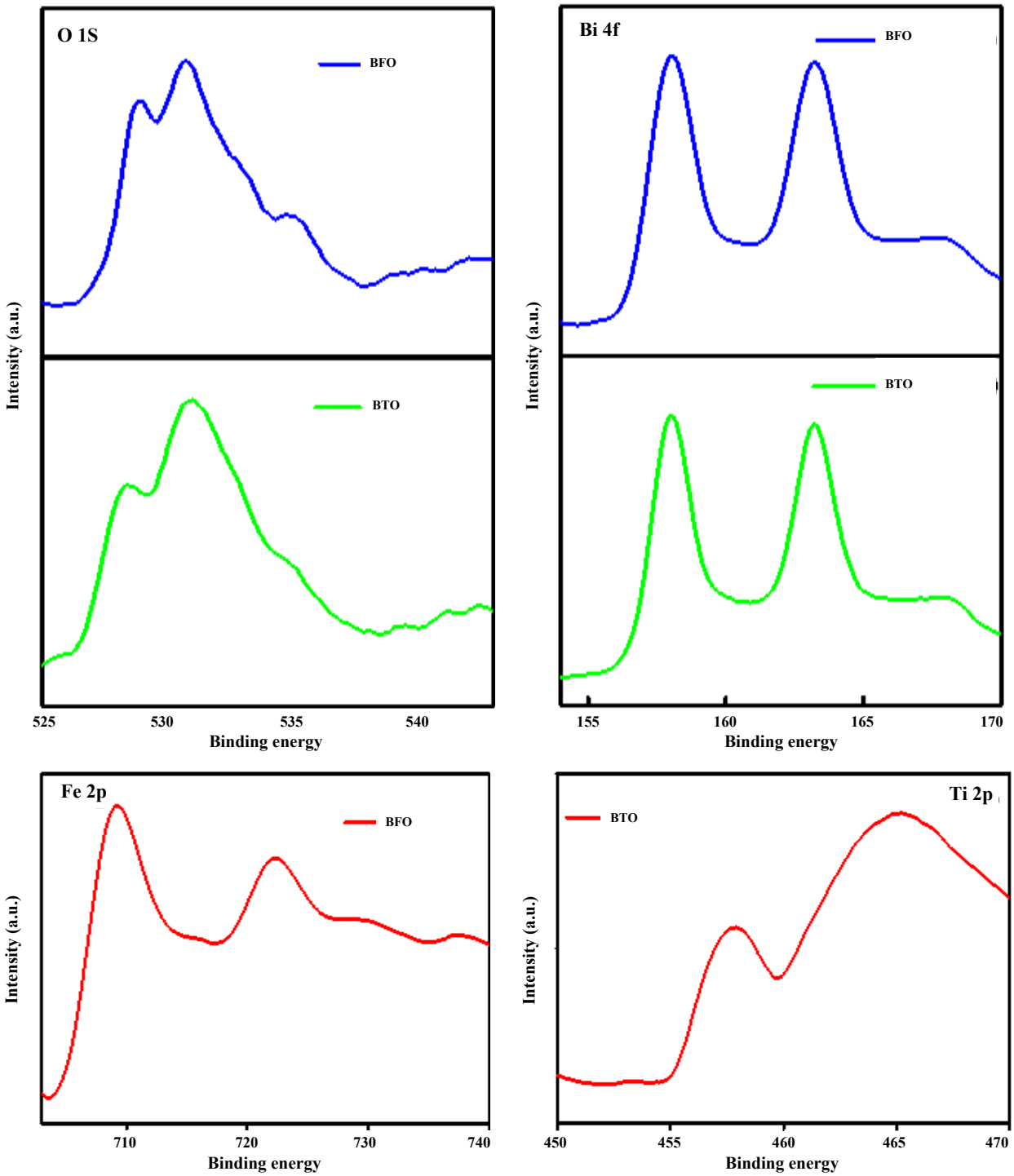

Figure 6. XPS spectra of BFO and BTO with the spin states representing O1s, Bi 4f, Fe 2p, and Ti 2p.

For BFO the Bi 4f state into the $4f_{5/2}$ and $4f_{7/2}$ peaks, located at binding energies of 163.2 eV and 158.1 eV, respectively. This doublet peak in the Bi 4f spectrum confirms the presence of pure Bi^{3+} in the BFO and rules out the existence of metallic Bi. The XPS spectra for the Fe 2p energy state. The Fe 2p spectrum is resolved into two peaks corresponding to $2p_{3/2}$ (609.3 eV) and $2p_{1/2}$ (722.3 eV). Additionally, a satellite peak appears at 718.5 eV, which is 7.9 eV above the $2p_{3/2}$ peak. These results unequivocally indicate that the oxidation state of Fe is Fe^{3+}. The XPS spectra for the O 1s energy state, showing two peaks at binding energies of 530.9 eV and 529.9 eV, which correspond to O^{2-} ions in the lattice. The higher-intensity peak at 530.9 eV represents the ideal lattice oxygen state, while the lower-intensity peak at 529.9 eV suggests a slight deviation from perfect stoichiometry. This deviation arises due to annealing, a process that plays a critical role in transitioning the structure to a single-phase BFO, as confirmed by XRD patterns. The Bi-rich phase, $Bi_{25}FeO_{39}$, disappears upon annealing in an oxygen atmosphere, transforming into the stoichiometric BFO phase. The smaller XPS peak at 529.9 eV reflects the reorientation of atoms during annealing, which adjusts the charge balance within the lattice paraphrase [36,37].

3.2 Photocatalytic activity

The photocatalytic performance of synthesized BFO and BTO were evaluated for the degradation of MB and MG under solar light with 4000 $W \cdot h \cdot m^{-2}$ insolation. To achieve adsorption-desorption equilibrium, the dye solution and catalyst were mixed and kept in the dark for about 30 min. The percentage of dye removal was determined using Equation (1), the variation of C_t/C_0 (with $C_0 = 20$ ppm) over time (t) for BFO and BTO and a catalyst dose of 20 mg is shown in Figure 7. As indicated, the materials displayed minimal adsorption in the dark. BFO exhibited the highest degradation efficiency under light, achieving ≈76% degradation of MB and ≈86% degradation of MG within 90 min and ≈78% degradation of MB and ≈82% degradation of MG within 60 min for BTO. Minimal dye degradation occurred in the dark, highlighting the necessity of solar light for effective dye degradation. BFO demonstrated a superior adsorption capacity for dye molecules due to its greater number of active sites [38]. To further explore the degradation performance, the catalyst was tested under various conditions. The effects of parameters like pH, catalyst dose, dye concentration, and irradiation time on degradation efficiency are discussed.

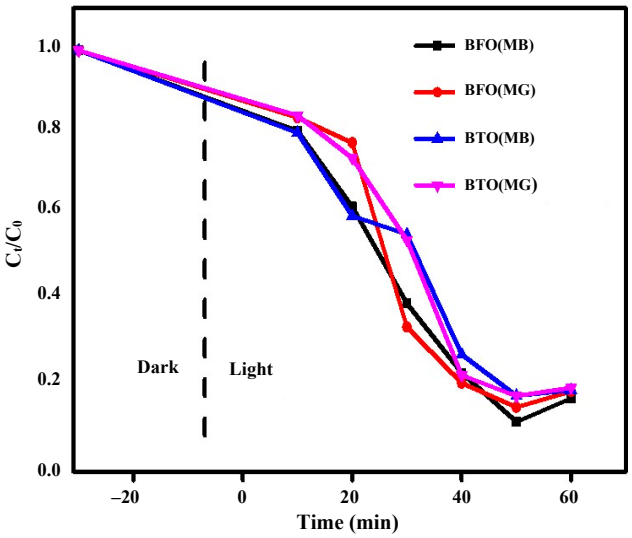

Figure 7. Photocatalytic degradation of MB and MG by BFO and BTO over time.

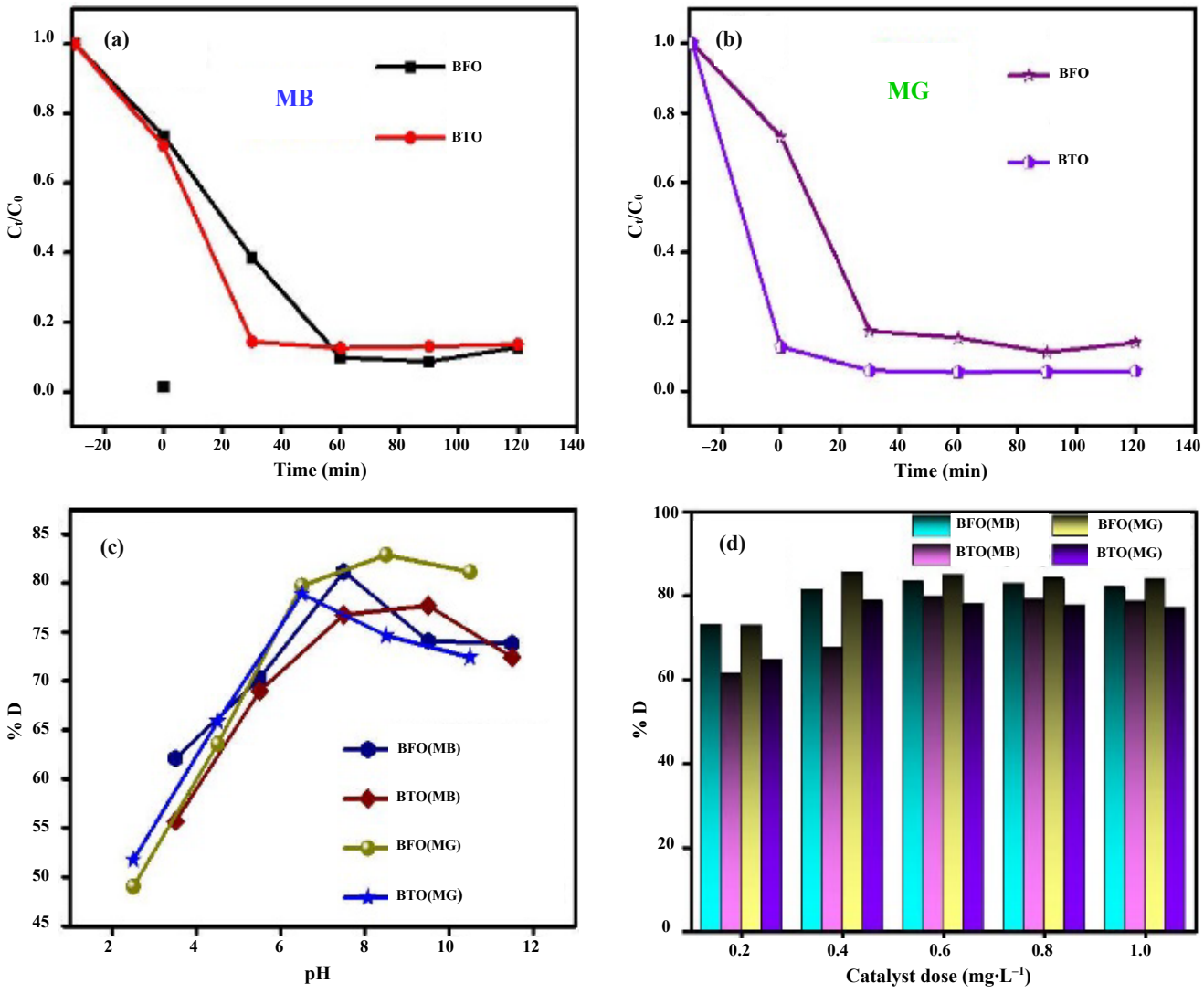

Figure 8. % age degradation of MB and MG for BFO and BTO. Agitation of time MB (a), MG (b). Effect of pH (c), and catalyst dosage (d).

The photocatalytic degradation of methylene blue (MB) and methylene green (MG) dyes by the synthesized perovskite nanoparticles was tested under sunlight. Control tests without BFO or BTO photocatalysts (Figure 8(a-b) showed that the dye concentration (5 mg·L^{-1}) remained stable, indicating the dyes' resistance to degradation. However, the addition of 40 mg of photocatalysts led to effective dye breakdown. The dye degradation efficiency of MB and MG (5 mg·L^{-1}) using 20 mg of BFO and BTO nanoparticles was studied under varying pH levels (3 to 12) with solar irradiation, as shown in Figure 8(c). The pH of the solution plays a crucial role in influencing electrostatic interactions between the catalyst, dye molecules, and reactive oxygen species (ROSs), which significantly impacts the degradation process [39].The study found that malachite green (MG) degradation was highest at pH 8.5 for BFO and pH 6.5 for BTO. Degradation efficiency peaked in basic conditions, with the process completing within 90 min for BFO and 60 min for BTO. Approximately 82% of MG was degraded using BFO and 78% using BTO, while 86% and 76% of methylene blue (MB) were degraded under similar conditions. Basic conditions enhance hydroxyl radical generation, aiding degradation. Additionally, increasing catalyst loading from 20 mg to 80 mg at a neutral pH improved dye degradation rates from about 60% to 86%, attributed to more active sites and increased radical production, as shown in Figure 8(d) [40].

Figure 9(a-d) show the reduction in absorbance of 100 mL MB and MG dye solutions over time at neutral pH, indicating dye degradation. For MG, 40 mg of BFO catalyst was used over 90 min, while MB was treated with 60 mg of BFO for 90 min, and 40 mg of BTO was applied for 60 min. The degradation kinetics of 5 mg·L^{-1} MG and MB dyes under neutral conditions were analyzed using a pseudo-first-order kinetic model with 60 mg and 40 mg of BFO and BTO photocatalysts, respectively shown in Figure 10(a-d). This model is represented as:

$$\ln (C_0/C) = kt \quad (5)$$

In this model, 'k' represents the rate constant, 't' denotes the irradiation time, and 'C_0' and 'C' stand for the dye concentrations before and after sunlight exposure, respectively [41]. The observed linear correlation between ln (C_0/C) and time, combined with an R^2 value nearing one, verifies that the dye degradation process follows first-order kinetics [42,43].

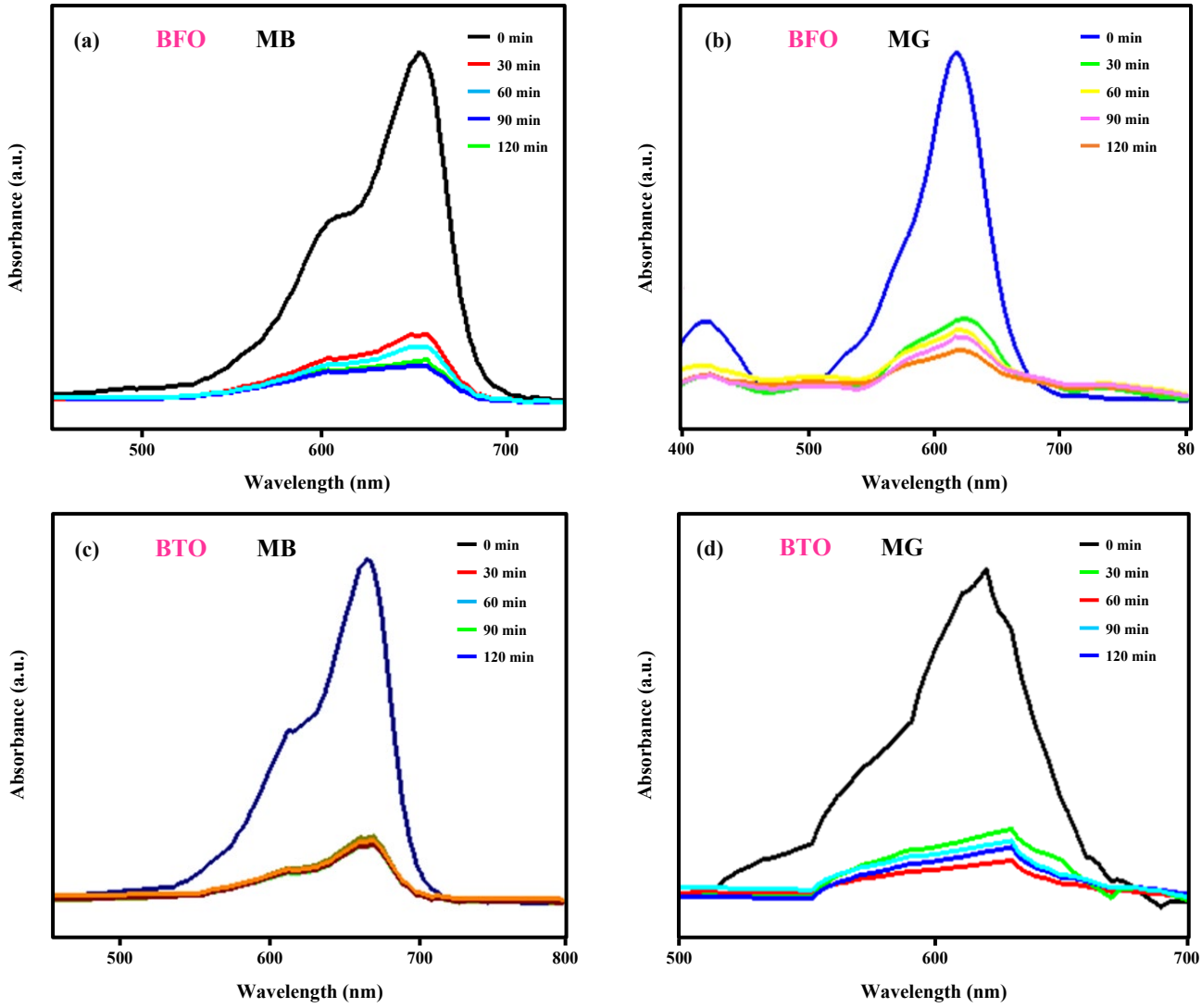

Figure 9. % degradation with time for BFO: MB (a) and MG (b), and for BTO: MB (c) and MG (d).

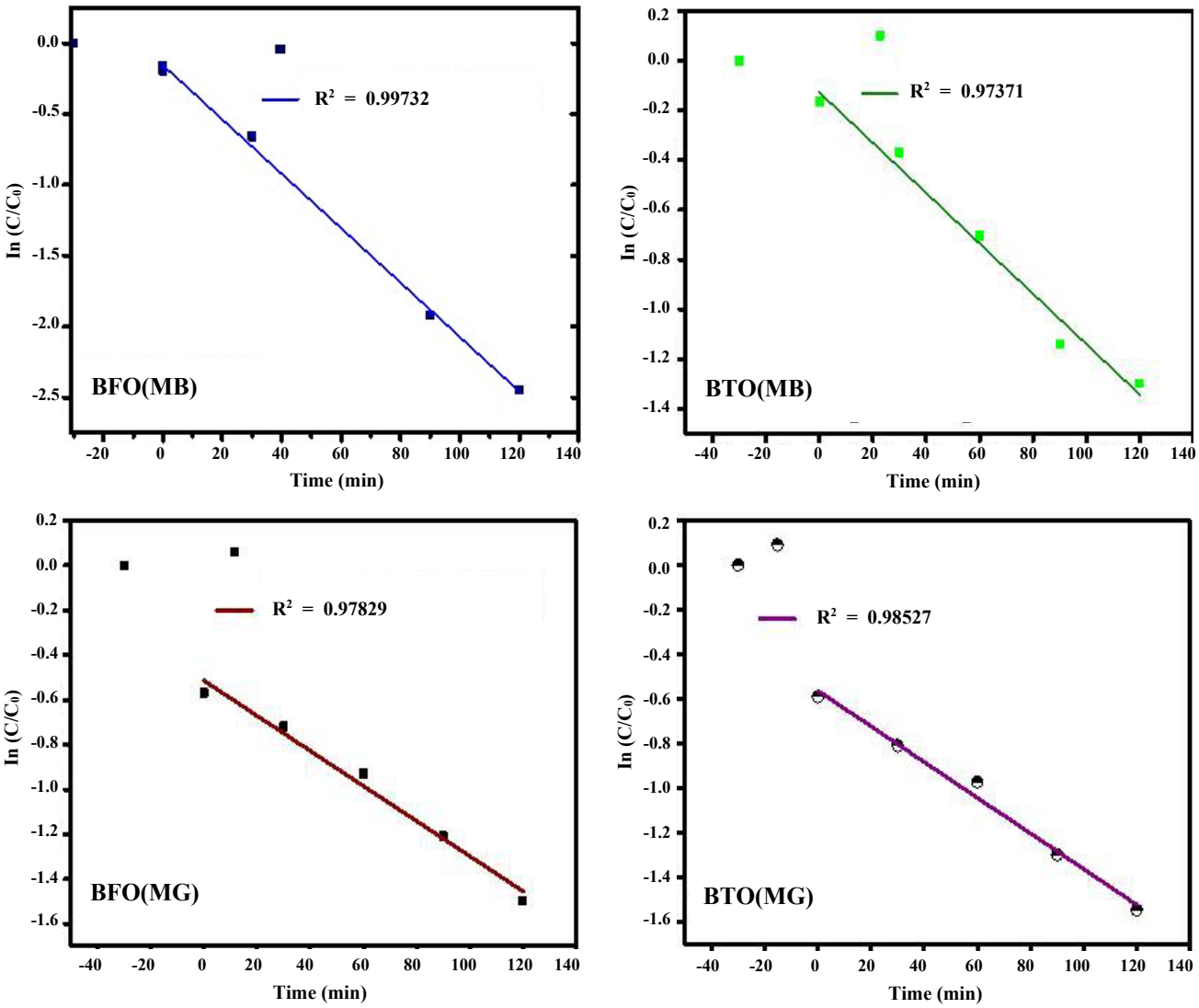

Figure 10. Kinetic studies of photocatalytic degradation by BFO towards: MB (a) and MG (b), and by BTO towards: MB (c) and MG (d).

Total Organic Carbon (TOC) measurements were used to evaluate the mineralization of MB and MG through photocatalysis. Figure 11 (a-b) present the TOC removal rates for MB and MG using BFO and BTO photocatalysts. The results showed that the TOC removal rate for both MB and MG increased with irradiation time, followed by a slight decrease after a certain period. The removal rates reached 84% (BFO) and 79% (BTO) for MB, and 86% (BFO) and 78% (BTO) for MG, respectively. This indicates that BFO and BTO facilitate almost complete degradation of these compounds, with some residual carbon remaining. These findings demonstrate that both BFO and BTO not only enhance the degradation efficiency of MB and MG but also improve their mineralization capabilities [37].

The stability and reusability of the perovskite photocatalysts were evaluated over five cycles under sunlight, as illustrated in Figure 12(a-b). After each cycle, the catalysts were recovered by centrifugation, washed, and dried at 70°C. Histogram results showed that for methylene blue (MB), BFO's degradation efficiency dropped from 80% to 54%, while BTO's declined from 71% to 49% over five cycles. For malachite green (MG), BFO's efficiency decreased from 80% to 69%, and BTO's from 76% to 63%. The decline in efficiency is likely due to slight catalyst loss during recovery. Several reactive species, including superoxide anion radicals ($O_2^{\bullet-}$), hydroxyl radicals ($^{\bullet}OH$), and photogenerated holes (h^+), are capable of degrading organic compounds. To explore the photocatalytic mechanism and identify the primary reactive species involved in the degradation of dye, a strategy using different scavengers was employed the effect of scavenger concentration was also assessed Figure 12(c-d). Notably, higher scavenger concentrations did not inhibit photodegradation, potentially due to other factors such as enhanced dye adsorption onto the photocatalyst surface EDTA scavenged holes (h^+), BQ scavenged superoxide radicals ($O_2^{\bullet-}$), and IPA scavenged hydroxyl radicals ($OH^{\bullet}$). Figure 12(c-d) show that EDTA slightly reduced photocatalytic efficiency, while BQ and IPA caused significant reductions. These results indicate that superoxide and hydroxyl radicals are crucial to the degradation process [44]. This result confirms that h^+ is the primary reactive species driving photodegradation, followed by $O_2^{\bullet-}$ with a moderate contribution and $^{\bullet}OH$ with a minor contribution in case of MB while in case of MG $^{\bullet}OH$ with a moderate contribution, and $O_2^{\bullet-}$ with a minor contribution, respectively.

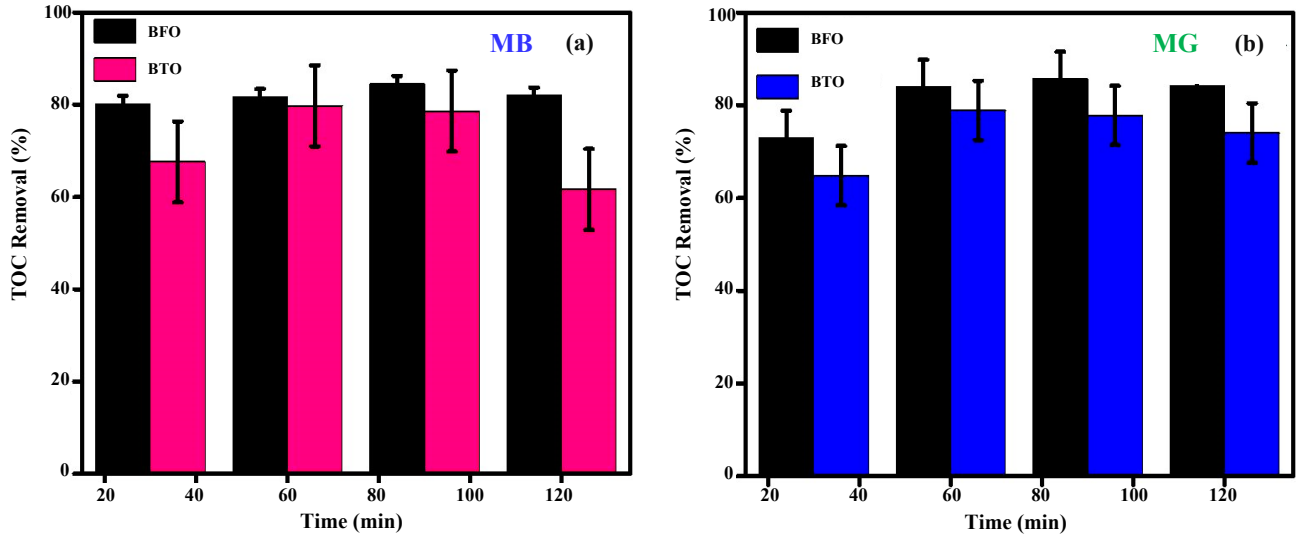

Figure 11. TOC removal rate of MB (a) and MG (b) using BFO and BTO photocatalysts.

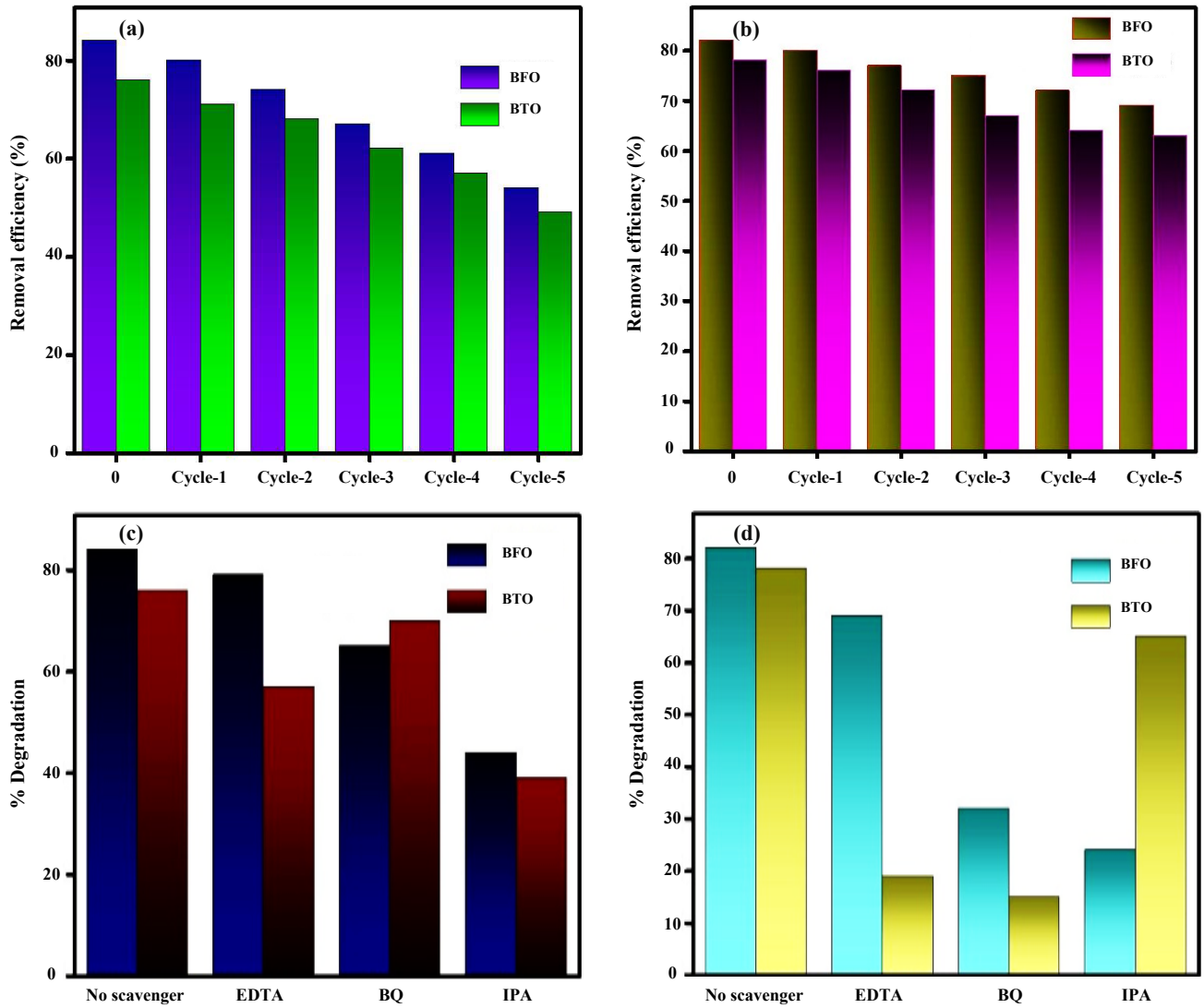

Figure 12. Recyclability test for BFO and BTO nanocomposites with MB (a), and MG (b), Scavenger test for synthesized BFO and BTO nanoparticles with MB (c), and MG (d).

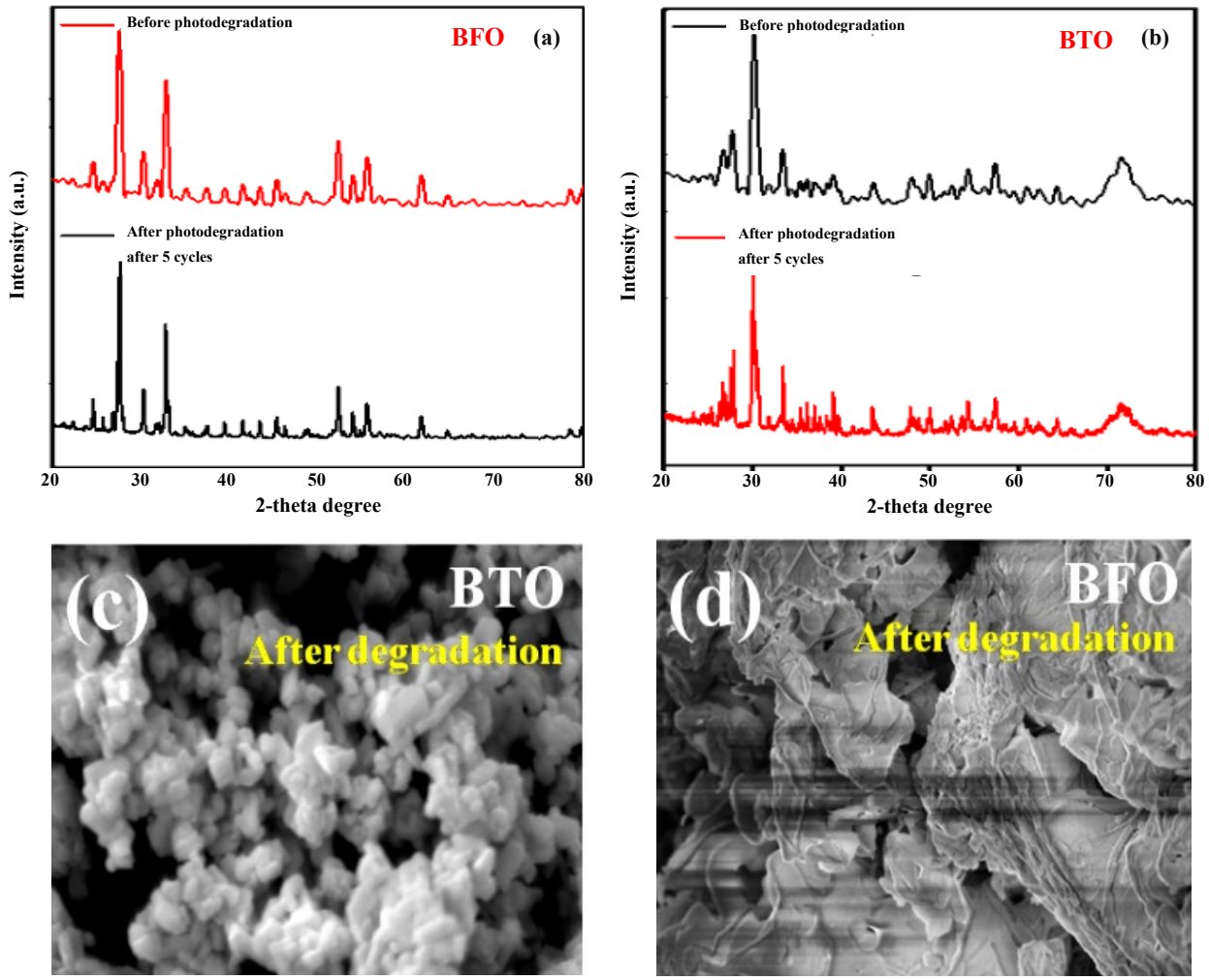

Figure 13. XRD patterns after five cycles of solar light irradiation for BFO (a) and BTO (b). SEM images after five cycles of solar light irradiation for BFO (c) and BTO (d).

In Figure 10 The XRD spectra of the samples before and after five-cycle degradation reveal no significant changes in their major peaks, indicating structural stability. However, some additional peaks emerge after degradation, which may suggest the formation of new phases or minor structural changes for BFO and BTO in Figure 13(a-b). Similarly, the SEM images exhibit flake-like structures for the BFO phase in Figure 13(c) and plate-like morphology for the BTO phase in Figure 13(d), consistent with their respective characteristics.

Scheme 2 presents a proposed mechanism for the photocatalytic activity of the synthesized BFO and BTO nanoparticles under sunlight. BFO's smaller band gap of 2.2 eV enables absorption in the visible region of the solar spectrum, allowing it to harness more sunlight compared to materials with larger band gaps that are limited to UV light. This enhances electron-hole pair generation, increasing charge carriers for redox reactions. By using the mott schottky analysis method by using Equation (4) and the result found that ECB 0.34 eV and EVB 2.52 eV for BFO and ECB 0.64 eV and EVB 3.54 eV for BTO respectively. The conduction band (CB) should be more negative than the redox potential of oxygen reduction to produce the super oxide radicals ($O_2^{-\bullet}$). The valence should be more positive than the redox potential of water oxidation to generate hydroxyl radicals ($^{\bullet}OH$). Additionally, the CB and VB should align with the redox potentials of the dye molecules for effective photocatalytic degradation. When exposed to sunlight, electrons and holes are generated in the conduction and valence bands, respectively. The electrons migrate to the surface, where they form superoxide radicals ($O_2^{\bullet-}$) by reacting with absorbed oxygen. These superoxide radicals interact with h^+ ions to produce hydrogen peroxide, which, in turn, generates active hydroxyl radicals when reacting with valence electrons. The holes react with water to produce hydroxyl ($OH^{\bullet}$) radicals. These electron-hole pairs are critical for photocatalytic processes, as they drive the redox reactions required for dye degradation and reactive oxygen species (ROS) production [45]. The study's findings, compared with previous data, show that the synthesized materials demonstrate strong photocatalytic capabilities for dye degradation, as summarized in Table 2-3.The equations governing the degradation mechanism are provided below.

$$\text{Catalyst} + hv \rightarrow e^-(CB) + h^+(VB) \quad (6)$$

$$O_2 + e^-(CB) \rightarrow O_2^{\bullet -} \quad (7)$$

$$h^+(VB) + H_2O \rightarrow OH^{\bullet} + H^+ \quad (8)$$

$$(MG, MB) + O_2^{\bullet -} + OH^{\bullet} \rightarrow H_2O \quad (9)$$

Table 2. Comparison table of previously reported photocatalysts with this photocatalysts.

Sl. No.	Perovskite	Dye	Band gap [eV]	Time [min]	%D	Ref.
1	$SrTiO_3$	Rhodamine B, Methylene blue	3.20	120	88, 92	[46]
2	$NiMnO_3$	Bromophenol blue	3.39	75	80	[47]
3	$BaTiO_3$	Methylene blue	2.90	180	92.8	[48]
4	Bi_2MoO_6	Methylene blue, Malachite green, Rhodamine B, Gentian violet	2.56	60	86, 97, 55, 82	[49]
5	$MgTiO_3$	Methylene blue, Rhodamine B, MO, and Congo red	2.80	180	89.7, 80.4, 79.4, and 79.4	[50]
6	$SrZrO_3$	Methylene blue	5.31	120	80.1	[51]
7	$CaTiO_3$	Methylene blue	2.67	240	87.1	[52]
8	$NdFeO_3$	Methylene blue	2.48	120	95	[53]
9	BFO	Methylene blue, Malachite green		90	≅80	Current study
10	BTO	Methylene blue, Malachite green		60	≅76	Current study

Table 3. Comparison table of previously reported BTO and BFO based photocatalyst

Sl. No.	Perovskite	Source	Dye	Time(min)	%D	Ref.
1	BFO	Visible light	Mordant blue 9	180	88.5	[54]
2	BFO	Sunlight	MB	180	89	[55]
3	BFO	Visible light	MB	120	98.49	[56]
4	BFO	Solar-driven	MB	180	73.2	[57]
5	Current study	Solar light	MB, MG	90	≅80	
6	BTO	Sunlight	RhB	50	50	[58]
7	BTO	Sunlight	RhB	120	91.3	[59]
8	BTO	Visible light	MO	240	96	[60]
9	BTO	Visible light	RhB	240	98	[61]
10	Current study	Solar light	MB, MG	60	≅76	

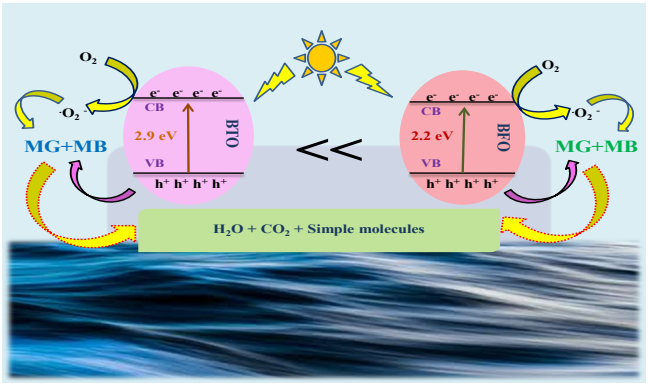

Scheme 3. Proposed mechanism for the photo-degradation of MB and MG dyes using BFO and BTO photocatalysts.

4. Conclusion

BFO and BTO nanocomposites were successfully synthesized using the sol-gel method, and their properties were analyzed using techniques such as XRD, SEM, TEM, EDAX, FTIR, and UV-DRS. XRD and SEM results showed that BFO and BTO have rhombohedral and orthorhombic crystal structures, respectively, with BFO particles having a uniform flake-like surface and BTO exhibiting a plate-like morphology. The band gaps for BFO and BTO were found to be 2.2 eV and 2.9 eV, respectively. Photocatalytic tests demonstrated that both materials effectively degraded MB and MG dyes under sunlight, with BFO showing higher efficiency than BTO. The BFO catalyst also exhibited excellent recyclability, maintaining around 80% efficiency after multiple cycles. Superoxide ($^{\bullet}O_2^-$) and hydroxyl ($^{\bullet}OH$) radicals were identified as the primary agents driving the degradation process, with minimal contribution from photo-excited holes (h^+).

Acknowledgements

The authors are appreciative to the department of chemistry at ITER, Siksha 'O' Anusandhan (Deemed to Be University), Bhubaneswar for providing laboratory space for this work. We thank various research centers, including Kalinga Institute of Industrial Technology and National Institute of Technology Rourkela, for sharing their analytical techniques.

Reference

[1] C. Liu, J. Zhang, W. Wang, L. Chen, and M. Zhu, "Progress in the synthesis and applications of N-rich carbon nitride (C_3N_5)-based catalysts in environmental and energy catalysis," *Surfaces and Interfaces*, vol. 42, p. 103491, 2023.

[2] J. Zhang, G. Yu, C. Yang, and S. Li, "Recent progress on S-scheme heterojunction strategy enabling polymer carbon nitrides C_3N_4 and C_3N_5 enhanced photocatalysis in energy conversion and environmental remediation," *Current Opinion in Chemical Engineering*, vol. 45, p. 101040, 2024.

[3] Haruna, I. Abdulkadir, and S. O. Idris, "Effect of annealing temperature on the synthesis and photocatalytic properties of $Bi_{0.65}K_{0.2}Ba_{0.15}FeO_3$ perovskite-like nanoparticle synthesized by sol-gel method," *Beni-Suef University Journal of Basic and Applied Sciences*, vol. 9, no. 1, 2020.

[4] M. A. El-Bendary, M. E. Fawzy, M. Abdelraof, M. El-Sedik, and M. A. Allam, "Efficient malachite green biodegradation by Pseudomonas plecoglossicide MG^2: Process optimization, application in bioreactors, and degradation pathway," *Microbial Cell Factories*, vol. 22, no. 1, 2023.

[5] Z. Kalaycıoğlu, B. Ö. Uysal, Ö. Pekcan, and F. B. Erim, "Efficient photocatalytic degradation of methylene blue dye from aqueous solution with cerium oxide nanoparticles and graphene oxide-doped polyacrylamide," *ACS Omega*, vol. 8, no. 14, pp. 13004-13015, 2023.

[6] P. K. Panda, R. Pattanaik, S. Mishra, D. Pradhan, and S. K. Dash, "Superior photocatalytic degradation of MB dye using $BiVO_4$ nanoparticles under solar light irradiation," *Materials Today Proceedings*, 2023.

[7] S. Li, C. You, K. Rong, C. Zhuang, X. Chen, and B. Zhang, "Chemically bonded $Mn_{0.5}Cd_{0.5}S$/BiOBr S-scheme photocatalyst with rich oxygen vacancies for improved photocatalytic decontamination performance," *Advanced Powder Materials*, vol. 3, no. 3, p. 100183, 2024.

[8] C. Shen, X. Li, B. Xue, D. Feng, Y. Liu, F. Yang, M. Zhang, and S. Li, "Surface plasmon effect combined with S-scheme charge migration in flower-like Ag/$Ag_6Si_2O_7$/$Bi_{12}O_{17}Cl_2$ enables efficient photocatalytic antibiotic degradation," *Applied Surface Science*, vol. 679, p. 161303, 2024.

[9] S. Li, C. You, Q. Xue, Y. Zhao, F. Yang, Y. Liu, L. Bai, M. Zhang, and C. Zhuang, "Carbon quantum dots and interfacial chemical bond synergistically modulated S-scheme $Mn_{0.5}Cd_{0.5}S$/BiOBr photocatalyst for efficient water purification," *Journal of Material Science and Technology*, vol. 214, pp. 255-265, 2024

[10] G. Pirgholi-Givi, S. Farjami-Shayesteh, and Y. Azizian-Kalandaragh, "The influence of preparation parameters on the photocatalytic performance of mixed bismuth titanate-based nanostructures," *Physica B Condensed Matter*, vol. 575, p. 311572, 2019.

[11] L. Mohanty, D. S. Pattanayak, R. Singhal, D. Pradhan, and S. K. Dash, "Enhanced photocatalytic degradation of rhodamine B and malachite green employing $BiFeO_3$/g-C_3N_4 nanocomposites: An efficient visible-light photocatalyst," *Inorganic Chemistry Communications*, vol. 138, p. 109286, 2022.

[12] N. Anu, and K. Yadav, "Optical and dielectric properties of $Bi_2Ti_2O_7$/$Bi_4Ti_3O_{12}$ nanocomposite," *Materials Today Proceedings*, vol. 28, pp. 153-157, 2020.

[13] Y. Geng, X. Zhang, and F. Wang, "Investigation of the physical characteristics of $Bi_4Ti_3O_{12}$, $Bi_2Ti_4O_{11}$, $Bi_{12}TiO_{20}$, $Bi_2Ti_2O_7$ ternary semiconductors," *Materials Science in Semiconductor Processing*, vol. 181, p. 108658, 2024.

[14] R. Pattanaik, D. Pradhan, and S. K. Dash, "A brief review on solar light assisted photocatalytic degradation of dyes using double/layered perovskites," *Current Nanoscience*, vol. 20, 2024.

[15] S. Xu, W. Shangguan, J. Yuan, J. Shi, and M. Chen, "Photocatalytic properties of bismuth titanate $Bi_{12}TiO_{20}$ prepared by co-precipitation processing," *Materials Science and Engineering B*, vol. 137, no. 1-3, pp. 108-111, 2006.

[16] T. Cheng, Q. Ma, H. Gao, S. Meng, Z. Lu, S.-F. Wang, Z. Yi, X. Wu, G. Liu, X. Wang, and H. Yang, "Enhanced photocatalytic activity, mechanism and potential application of Idoped-$Bi_4Ti_3O_{12}$ photocatalysts," *Materials Today Chemistry*, vol. 23, p. 100750, 2022.

[17] N. D. M. Ridzuan *et al.*, "Photocatalytic heterostructures-based $BiFeO_3$ embedded liquid natural rubber (LNR) for highly removal of cationic dye under direct sunlight," *Journal of Environmental Chemical Engineering*, vol. 8, no. 5, p. 104152, 2020.

[18] S. E. Ali, "Influence of preparation method on phase formation, structural and magnetic properties of $BiFeO_3$," *Journal of Electroceramics*, vol. 48, no. 2, pp. 95-101, 2022.

[19] K. Afroz, M. Moniruddin, N. Bakranov, S. Kudaibergenov, and N. Nuraje, "A heterojunction strategy to improve the visible light sensitive water splitting performance of photocatalytic materials," *Journal of Materials Chemistry A*, vol. 6, no. 44, pp. 21696-21718, 2018.

[20] R. He, D. Xu, B. Cheng, J. Yu, and W. Ho, "Review on nanoscale Bi-based photocatalysts," *Nanoscale Horizons*, vol. 3, no. 5, pp. 464-504, 2018.

[21] S. K. Badge and A. V. Deshpande, "Effect of pressure of pelletization on dielectric properties of bismuth titanate prepared by sol-gel synthesis," *Advanced Powder Technology*, vol. 29, no. 3, pp. 555-562, 2017.

[22] Y. Wu, Y. Zang, L. Xu, J. Wang, H. Jia, and F. Miao, "Synthesis of functional conjugated microporous polymer/TiO_2 nanocomposites and the mechanism of the photocatalytic degradation of organic pollutants," *Journal of Materials Science*, vol. 56, no. 13, pp. 7936-7950, 2021.

[23] Z. Chen, J. Hu, and X. He, "Piezoelectric and dielectric properties of $(Na_{0.5}K_{0.5})NbO_3$-$Bi_{0.5}(Na_{0.8}K_{0.2})0.5TiO_3$ lead-free ceramics," *Journal of the Ceramic Society of Japan*, vol. 116, no. 1353, pp. 661-663, 2008.

[24] F. Lin, Q. Yu, L. Deng, Z. Zhang, X.-Y. He, A. Liu, and W. Shi, "Effect of La/Cr codoping on structural transformation, leakage, dielectric and magnetic properties of $BiFeO_3$ ceramics," *Journal of Materials Science*, vol. 52, no. 12, pp. 7118-7129, 2017.

[25] M. Sivagami, and I. V. Asharani, "Phyto-mediated Ni/NiO NPs and their catalytic applications-a short review," *Inorganic Chemistry Communications*, vol. 145, p. 110054, 2022.

[26] M. E. Castillo, V. V. Shvartsman, D. Gobeljic, Y. Gao, J. Landers, H. Wende, and D. Lupascu, "Effect of particle size on ferroelectric and magnetic properties of $BiFeO_3$ nanopowders," *Nanotechnology*, vol. 24, no. 35, p. 355701, 2013.

[27] T. Xian, H. Yang, X. Shen, J. L. Jiang, Z. Q. Wei, and W. J. Feng, "Preparation of high-quality $BiFeO_3$ nanopowders via a polyacrylamide gel route," *Journal of Alloys and Compounds*, vol. 480, no. 2, pp. 889-892, 2009.

[28] P. Thiruramanathan, S. K. Sharma, S. Sankar, R. S. Ganesh, A. Marikani, and D. Y. Kim, "Synthesis of bismuth titanate (BTO) nanopowder and fabrication of microstrip rectangular patch antenna," *Applied Physics A*, vol. 122, no. 12, 2016.

[29] J. Zhu, M. Ye, and A. Han, "Preparation and microwave absorption properties of $BiFeO_3$ and $BiFeO_3$/PANI composites," *Journal of Materials Science Materials in Electronics*, vol. 28, no. 18, pp. 13350-13359, 2017.

[30] J. A. Dias, J. A. Oliveira, C. G. Renda, and M. R. Morelli, "Production of nanometric $Bi_4Ti_3O_{12}$ powders: From synthesis to optical and dielectric properties," *Materials Research*, vol. 21, no. 5, 2018.

[31] D. Hou, X. Hu, P. Hu, W. Zhang, M. Zhang, and Y. Huang, "$Bi_4Ti_3O_{12}$ nanofibers–BiOI nanosheets p–n junction: facile synthesis and enhanced visible-light photocatalytic activity," *Nanoscale*, vol. 5, no. 20, p. 9764, 2013.

[32] T. Hu, K. Dai, J. Zhang, and S. Chen, "Noble-metal-free Ni2P modified step-scheme $SnNb_2O_6$/CdS-diethylenetriamine for photocatalytic hydrogen production under broadband light irradiation," *Applied Catalysis B Environment and Energy*, vol. 269, p. 118844, 2020.

[33] J. H. Jang, K.-S. Jeon, S. Oh, H-J. Kim, T. Asahi, H. Masuhara, and M. Yoon,"Synthesis of Sn-porphyrin-intercalated trititanate nanofibers: optoelectronic properties and photocatalytic activities," *Chemistry of Materials*, vol. 19, no. 8, pp. 1984-1991, 2007.

[34] N. Sonu, S. Sharma, V. Dutta, P. Raizada, A. Singh, P. Singh, T. Ahamad, Q. V. Le, and V.-H. Hguyen, "Type-II heterojunction-based magnetic $ZnFe_2O_4$@$CuFe_2O_4$@SiO_2 photocatalyst for photodegradation of toxic dyes from wastewater," *Applied Nanoscience*, vol. 13, no. 5, pp. 3693-3707, 2022.

[35] L. Wang, W. Ma, Y. Fang, Y. Zhang, M. Jia, R. Li, and Y. Huang, "$Bi_4Ti_3O_{12}$ synthesized by high temperature solid phase method and it's visible catalytic activity," *Procedia Environmental Sciences*, vol. 18, pp. 547-558, 2013.

[36] P. M. Razad, S. Kasimedu, V. Ganesan, R. J. Choudhary, A. M. E. Raj, R. Devaraj, J. M. Nair, K. Mahalakshmi, M. M. Patidar, V. R. Sreelakshmi, M. Govindasamy, and S. Chinnappanadar, "Novel report on single phase $BiFeO_3$ nanorod layer synthesised rapidly by novel hot-wall spray pyrolysis system: evidence of high magnetization due to surface spins," *Journal of Materials Science Materials in Electronics*, vol. 28, no. 4, pp. 3217-3225, 2016.

[37] L. Mohanty, D. S. Pattanayak, R. Singhal, D. Pradhan, and S. K. Dash, "Enhanced photocatalytic degradation of rhodamine B and malachite green employing $BiFeO_3$/g-C_3N_4 nanocomposites: An efficient visible-light photocatalyst," *Inorganic Chemistry Communications*, vol. 138, p. 109286, 2022.

[38] D. Pradhan, L. Mohanty, R. Singhal, E. Falletta, and S. K. Dash, "Sustainable and solar light assisted photocatalytic degradation of MB and MG dyes by Co_3O_4/g-C_3N_4 nanocomposite," *Inorganic Chemistry Communications*, vol. 156, p. 111259, 2023.

[39] G. Pirgholi-Givi, Y. Azizian-Kalandaragh, and J. Farazin, "Comparison of the photocatalytic activity of perovskite structures: Bismuth, barium, and zinc titanate nanostructures for photodegradation of methylene blue from water," *Journal of Photochemistry and Photobiology a Chemistry*, vol. 408, p. 113104, 2020.

[40] D. Rosa, G. Manetta, and L. Di Palma, "Experimental assessment of the pH effect and ions on the photocatalytic activity of iron-doped titanium dioxide supported on polystyrene pellets: Batch and continuous tests," *Chemical Engineering Science*, vol. 291, p. 119918, 2024.

[41] Y. Chen, S. Xu, C. F. Wen, H. Zhang, T. Zhand, F. Lv, Y. Yue, and Z. Bian, "Unravelling the role of free radicals in photo-catalysis," *Chemistry - a European Journal*, vol. 30, no. 29, p. e202400001, 2024.

[42] M. F. A. Messih, M. A. Ahmed, A. Soltan, and S. S. Anis, "Synthesis and characterization of novel Ag/ZnO nanoparticles for photocatalytic degradation of methylene blue under UV and solar irradiation," *Journal of Physics and Chemistry of Solids*, vol. 135, p. 109086, 2019.

[43] D. Pradhan, S. K. Biswal, R. Pattanaik, N. Nayak, and S. K. Dash, "Strontium doped, a p-n heterojunctionTiO_2/Sr-Co_3O_4 composite for enhanced photocatalytic degradation of MG dye under solar light irradiation," *New Journal of Chemistry*, vol. 48, no. 38, pp. 16853-16868, 2024.

[44] D. Pradhan, S. K.Biswal, N. Nayak, R. Singhal, S. K. Beriha, R. Pattanaik, and S. K. Dash, "Bioinspired synthesis of transition metal-enhanced Co_3O_4 using mangifera indica leaves for photo-catalytic and energy storage applications," *ChemistrySelect*, vol. 9, no. 48, p. e202403211, 2024.

[45] D. Pradhan, S. K. Biswal, R. Pattanaik, N. Nayak, and S. K. Dash, "Strontium doped, a p-n heterojunctionTiO_2/Sr-Co_3O_4 composite for enhanced photocatalytic degradation of MG dye under solar light irradiation," *New Journal of Chemistry*, vol. 48, no. 38, pp. 16853-16868, 2024.

[46] L. D. Namade, S. S. Band, P. K. Pawar, A. R. Patil, R. S. Pedanekar, K. G. Managave, V. V. Ganbavle, and K. Y. Rajpure, "Ultraviolet light-driven degradation of organic dyes using $SrTiO_3$ photocatalytic nanoparticles," *Colloids and Surfaces a Physico-chemical and Engineering Aspects*, vol. 708, p. 135976, 2025.

[47] V. Jose, V. Jose, E. Kuruvilla, M. Arunkumar, A. S. Deepi, G. Srikesh, and A. S. Nesaraj "Facile chemical synthesis of Mg-doped $NiMnO_3$ perovskite based nano-structured materials: Application in photocatalysis and supercapacitors," *Inorganic Chemistry Communications*, vol. 156, p. 111205, 2023.

[48] H. Bantawal, and D. K. Bhat, "Hierarchical porous $BaTiO_3$ nano-hexagons as a visible light photocatalyst," *International Journal of Engineering & Technology*, vol. 7, no. 4.5, pp. 105-109, 2018.

[49] P. Zhu, R. Wang, M. Duan, Y. Chen, M. Hu, X. Luo, and H. Teng, "efficient adsorption and photocatalytic degradation of

dyes by AgI-Bi_2MoO_6/vermiculite composite under visible light," *ChemistrySelect*, vol. 4, no. 41, pp. 12022-12031, 2019.

[50] N. Kitchamsetti, P. N. Didwal, S. R. Mulani, M. S. Patil, and R. S. Devan, "Photocatalytic activity of $MnTiO_3$ perovskite nanodiscs for the removal of organic pollutants," *Heliyon*, vol. 7, no. 6, p. e07297, 2021.

[51] J. N. Tsaviv, I. S. Eneji, R. Sha'Ato, I. Ahemen, P. R. Jubu, and Y. Yusof, "Photodegradation, kinetics and non-linear error functions of methylene blue dye using $SrZrO_3$ Perovskite photocatalyst," *Heliyon*, vol. 10, no. 14, p. e34517, 2024.

[52] C. Karthikeyan, M. Thamima, and S. Karuppuchamy, "Dye removal efficiency of perovskite structured $CaTiO_3$ nanospheres prepared by microwave assisted method," *Materials Today Proceedings*, vol. 35, pp. 44-47, 2019.

[53] A. H. Shankara, J. S. Prabagar, T. Tenzin, S. Yadav, K. M. A. Kumar, and H. P. Shivaraju, "Facile synthesis of $NdFeO_3$ perovskite for photocatalytic degradation of organic dye and antibiotic," *Materials Today Proceedings*, vol. 75, pp. 15-23, 2022.

[54] J. Ćirković, A. Radojković, D. L.Golić, N. Tasić, M.Čizmić, G. Branković, and Z. Branković, "Visible-light photocatalytic degradation of Mordant Blue 9 by single-phase $BiFeO_3$ nanoparticles," *Journal of Environmental Chemical Engineering*, vol. 9, no. 1, p. 104587, 2020.

[55] S. Parida, J. Nanda, B. Sarangi, and R. Behera, "Plant extract mediated synthesis of $BiFeO_3$ nanoparticles for photocatalytic degradation of methylene blue dye," *Biomass Conversion and Biorefinery*, 2024.

[56] N. N. Mharsale, P. S. More, Y. B. Khollam, S. F. Shaikh, A. M. Al-Enizi, and S. R. Gadakh, "Visible light-induced photocatalytic degradation of methylene blue dye using pure phase bismuth ferrite nanoparticles," *Journal of Physics and Chemistry of Solids*, vol. 192, p. 112049, 2024.

[57] S. Bharathkumar, M. Sakar, and S. Balakumar, "Egg white-mediated synthesis of $BiFeO_3$ cubes and their enhanced photocatalytic degradation properties under solar irradiation," *Journal of Materials Science Materials in Electronics*, vol. 33, no. 16, pp. 12638-12647, 2022.

[58] S. Niu, R. Zhang, X. Zhang, J. Xiang, and C. Guo, "Morphology-dependent photocatalytic performance of $Bi_4Ti_3O_{12}$," *Ceramics International*, vol. 46, no. 5, pp. 6782-6786, 2019.

[59] P. Thiruramanathan, S. Manjula, N. Karthikeyan, R. Srinivasan, and V. Sivakumar, "Photodegradation behaviour of sol–gel synthesized $Bi_4Ti_3O_{12}$ for water pollution disinfection," *Materials Today Proceedings*, 2023.

[60] Y. Zhang, J. Gao, Z. Chen, and Z. Lu, "Enhanced photocatalytic performance of $Bi_4Ti_3O_{12}$ nanosheets synthesized by a self-catalyzed fast reaction process," *Ceramics International*, vol. 44, no. 18, pp. 23014-23023, 2018.

[61] A. R. Noviyanti, D. R. Eddy, M. D. Permana, and R. Risdiana, "Heterophase of bismuth titanate as a photocatalyst for rhodamine B degradation," *Trends in Sciences*, vol. 20, no. 10, p. 6147, 2023.